metals

MDPI

Article

Validation Study on the Statistical Size Effect in Cast Aluminium

Matthias Oberreiter *, Sebastian Pomberger, Martin Leitner and Michael Stoschka

Christian Doppler Laboratory for Manufacturing Process Based Component Design, Chair of Mechanical Engineering, Montanuniversität Leoben, Franz-Josef-Straße 18, 8700 Leoben, Austria; sebastian.pomberger@unileoben.ac.at (S.P.); martin.leitner@unileoben.ac.at (M.L.); michael.stoschka@unileoben.ac.at (M.S.)

* Correspondence: matthias.oberreiter@unileoben.ac.at; Tel.: +43-3842-402-1474

Received: 29 April 2020; Accepted: 22 May 2020; Published: 27 May 2020

Abstract: Imperfections due to the manufacturing process can significantly affect the local fatigue strength of the bulk material in cast aluminium alloys. Most components possess several sections of varying microstructure, whereat each of them may inherit a different highly-stressed volume (HSV). Even in cases of homogeneous local casting conditions, the statistical distribution parameters of failure causing defect sizes change significantly, since for a larger highly-stressed volume the probability for enlarged critical defects gets elevated. This impact of differing highly-stressed volume is commonly referred as statistical size effect. In this paper, the study of the statistical size effect on cast material considering partial highly-stressed volumes is based on the comparison of a reference volume V_0 and an arbitrary enlarged, but disconnected volume V_α utilizing another specimen geometry. Thus, the behaviour of disconnected highly-stressed volumes within one component in terms of fatigue strength and resulting defect distributions can be assessed. The experimental results show that doubling of the highly-stressed volume leads to a decrease in fatigue strength of 5% and shifts the defect distribution towards larger defect sizes. The highly-stressed volume is numerically determined whereat the applicable element size is gained by a parametric study. Finally, the validation with a prior developed fatigue strength assessment model by R. Aigner et al. leads to a conservative fatigue design with a deviation of only about 0.3% for cast aluminium alloy.

Keywords: aluminium casting; fatigue assessment; shrinkage porosity; statistical size effect; extreme value statistics; highly-stressed volume

1. Introduction

Complex cast aluminium parts possess a severely heterogeneous microstructure and therefore it is essential to consider its interaction with the highly stressed volume (HSV). The result of elevated highly stressed volumes in terms of cyclic loading is generally a reduced the fatigue strength. According to References [1,2], size effects can be classified into technological, geometrical, statistical and surface technology size effects. Larger components, respectively larger HSV, increase the probability of critical defect sizes, thus lessening the endurable fatigue strength. The aim of this work is the validation of the statistical size effect with consideration of the microstructural properties, as introduced as probabilistic design method for aluminium castings in References [3–5]. In general, the local fatigue strength correlates well with the dedicated microstructure because of the statistical distribution of the defects, apparent in preliminary studies [6–11]. Therefore, it is essential to consider the local pore size distribution in the fatigue design process. Fatigue initiating defects in cast parts can be described well with extreme value statistics, like the generalized extreme value distribution (GEV) or the Gumbel distribution [12–14]. Further methodologies to assess the statistical size effect with regard to volumetric

dependencies and highly stressed surface models are given in References [15–22]. In these latter cases, a highly stressed volume, which is defined as the volume with a particular percentage of the maximum stress node, is taken into account. One of these approaches is the volumetric model of Sonsino [16], who invokes the 90% highly-stressed volume V_{90} and the Weibull exponent κ to assess the size effect related fatigue strength, represented in Equation (1).

$$\frac{\sigma_{\mathrm{LLF},0}}{\sigma_{\mathrm{LLF},1}} = \left(\frac{V_{90,1}}{V_{90,0}}\right)^{\frac{1}{\kappa}} \tag{1}$$

In this equation, $\sigma_{LLF,0}$ and $\sigma_{LLF,1}$ represent the long-life fatigue strength of the highly-stressed volumes $V_{90,0}$ and $V_{90,1}$. The material dependent Weibull exponent κ specifies the slope in the double logarithmic σ_{LLF}-V_{α}-plot and therefore the reduction of the fatigue strength against the highly-stressed volume. Its value and can be taken either by a common guideline [23], which defines the parameter as $\kappa = 10$ for aluminium castings, or be calculated dependent on the probability distribution of the fatigue data, represented by T_S [17], see Equation (2). In this equation, T_S is the scatter index of the high cycle fatigue region at ten million load cycles, defined as the stress ratio between a 10% and 90% probability of survival. In Reference [24], Sonsino proposed a threshold volume $V_{\infty} = 8000$ mm^3 for cast aluminium material, implying that no further noticeable decrease in fatigue strength may be observed.

$$\kappa = \frac{1.3151}{log(T_s)}. \tag{2}$$

The weakest link model of Weibull [25] as well as the discussed volumetric model are in good accordance to the experimental fatigue data [26]. Studies on artificial defects in References [27,28] exhibit that the highly-stressed volume approach is more suitable to investigate the statistical size effect. Both, the common engineering guideline [23] and short-crack growth findings in Reference [1] recommend a highly stressed surface model but refer additionally to highly-stressed volume models. Hence, the model of Sonsino [16] is used in this study for the validation of the statistical size effect. Kitagawa and Takahashi recommended in Reference [29] that the long life fatigue strength σ_{LLF} can be related to a dedicated crack length a, respectively to equivalent defect size, which can be defined as equivalent circle diameter (ECD) or by the equivalent edge length of a square ($\sqrt{area}$), see Equation (3). The sound applicability of the model from Kitagawa and Takahashi has been proven in several studies, see References [3,4,7,30–36].

$$\Delta\sigma_{LLF} = \frac{\Delta K_{th,lc}}{Y\sqrt{\pi a}}. \tag{3}$$

In this equation, $\Delta K_{th,lc}$ is the long crack threshold and Y a geometry factor depending on the geometrical shape and location of the defects, as discussed in preliminary studies such as that in Reference [37]. The design strength is limited on the one hand by the long life fatigue strength of the near defect free material $\Delta\sigma_0$, evaluated at specimens with hot isostatic pressed (HIP) condition with T6 heat treatment (HIP + T6). Otherwise, the fracture mechanical approach takes into account the long crack threshold value $\Delta K_{th,lc}$ and the effective crack threshold value $\Delta K_{th,eff}$. These crack threshold values come into effect for flaw sizes becoming larger than a intrinsic crack length $a_{0,eff}$, respectively $a_{0,lc}$. Further improvements of the Kitagawa Takahashi diagram by El Haddad [38,39] and Chapetti [40] are considering the crack resistance curve. A schematic representation of the Kitagawa Takahaschi diagram (KTD) and its modifications are given in Figure 1.

The crack extension from the intrinsic threshold $\Delta K_{th,eff}$ to the long crack threshold $\Delta K_{th,lc}$ can be represented by applying the cyclic crack resistance curve (R-cureve), as introduced by Reference [41]. The build-up of the crack resistance from the intrinsic $\Delta K_{th,eff}$ to the long crack threshold $\Delta K_{th,lc}$ with elevating crack length is caused by crack closure effects [42,43], whereat a premature contact of the crack faces generally leads to a minor real effective load ΔK_{eff} for further crack propagation, see Equation (4).

$$\Delta K_{eff} = K_{max} - K_{op}. \tag{4}$$

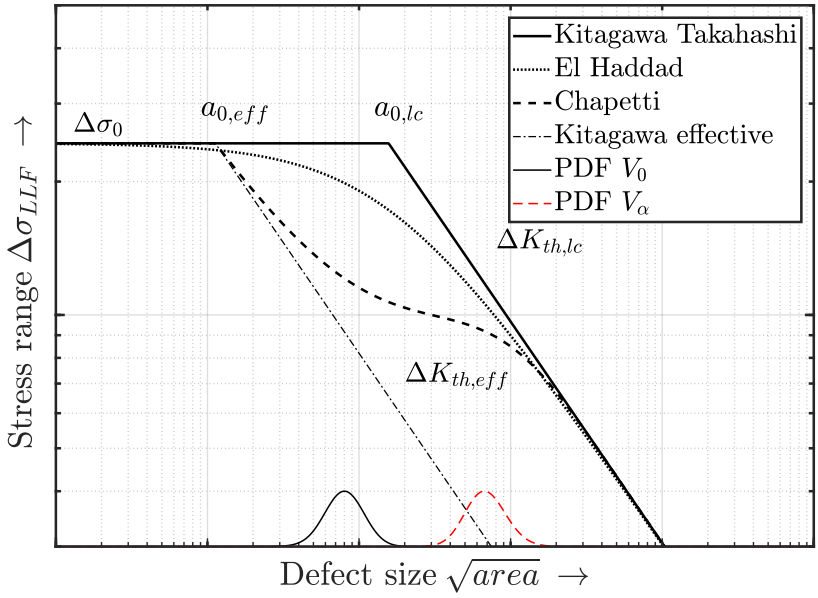

Figure 1. Schematic set up of the Kitagawa Takahashi diagram with its modifications and exemplary defect distributions of a volume V_0 and an enhanced volume V_α.

Crack closure effects can be classified into plasticity-, roughness-, and oxide-induced crack closure fractions as the most pronounced ones, whereat an explicit separation of these effects is not possible [44–49]. Maierhofer recommended in Reference [41] a procedure to describe the R-curve in a unified manner as given in Equation (5).

$$\Delta K_{th,\Delta a} = \Delta K_{th,eff} + \left(\Delta K_{th,lc} - \Delta K_{th,eff}\right)\left[1 - \sum_{i=0}^{n} \nu_i \cdot \exp\left(-\frac{\Delta a}{l_i}\right)\right], \tag{5}$$

with

$$\sum_{i=0}^{n} \nu_i \equiv 1.$$

In this equation, the crack closure effects are considered using the parameters ν_i and l_i, implying that if the crack reaches length l_i the corresponding closure effect ν_i is completely developed. By inserting Equation (5) in Equation (3), the cyclic R-curve can be implemented in the KTD whereby this extension of the KTD is useful to assess both, physically short and long, cracks. Therein, the crack length a is substituted by the equivalent defect size $\sqrt{area}$. Murakami introduced in Reference [50] the $\sqrt{area}$-parameter, which is the cross section of a defect in respect to the load direction. According to a study in Reference [51], the stress field surrounding the defect correlates well with the $\sqrt{area}$-parameter. Hence, this parameter is used to assess the crack initiating defects. Preliminary studies [5,52,53] contributed to the measurement methods of defects in cast aluminium alloys, as also applied within this study.

In References [12–14,54] it was shown that the statistical distribution of defect sizes follow an extreme value distribution. The Generalized Extreme Value (GEV) distribution includes the Frechet, Gumbel and Weibull distribution [55] and is applicable for characterizing crack initiating defect sizes [12]. Its cumulative distribution function (CDF), see Equation (6), is defined by three parameters, named as location μ, scale δ and shape ξ parameter which can be estimated by using the maximum likelihood method, applied in the studies [12,53,56,57]. The shape parameter ξ determines the type of extreme value distribution, differentiating between three cases: $\xi \to 0$ indicates a Gumbel, $\xi < 0$ a Weibull and $\xi > 0$ a Fréchet distribution, see Reference [13].

As published in a previous study [3], the CDF of an α-times enlarged volume V_α of the defect distribution P^α can be derived based on the distribution of the reference volume V_0 according to Reference [58], expressed in Equations (6)–(12).

$$V_0 \sim P(\sqrt{area}; \mu, \delta, \xi) = \exp\left\{-\left[1+\xi\left(\frac{\sqrt{area}-\mu}{\delta}\right)\right]^{-\frac{1}{\xi}}\right\} \tag{6}$$

$$V_\alpha \sim P^\alpha, \tag{7}$$

with

$$\xi_\alpha = \xi \tag{8}$$

$$\delta_\alpha = \delta \cdot \alpha^\xi \tag{9}$$

$$\mu_\alpha = \mu + \frac{\delta}{\xi} \cdot \left(\alpha^\xi - 1\right), \tag{10}$$

which leads to

$$P^\alpha = \exp\left\{-\left[1+\xi\left(\frac{\sqrt{area}-(\mu+\frac{\delta}{\xi}(\alpha^\xi-1))}{\delta\alpha^\xi}\right)\right]^{-\frac{1}{\xi}}\right\} \tag{11}$$

$$V_\alpha \sim P\left(\sqrt{area}; \mu + \frac{\delta}{\xi}\left(\alpha^\xi - 1\right), \delta\alpha^\xi, \xi\right). \tag{12}$$

Detailed methodologies to calculate the maximum defect in geometries with enlarged HSV are given in References [59,60], whereat it is shown that the most extremal defects are commonly Gumbel distributed, applied in Equation (13), using the location parameter μ and scale parameter δ.

$$P(\sqrt{area}) = exp\left\{-exp\left[-\frac{\sqrt{area}-\mu}{\delta}\right]\right\}. \tag{13}$$

Now the size of a critical defect in an enlarged control volume V_α, which is considered by the ratio of the enlarged volume V_α divided by the reference volume V_0, can be calculated by Equation (14).

$$\sqrt{area}(\alpha) = \mu - \delta \cdot ln\left[-ln\left(1-\frac{1}{\alpha}\right)\right] \tag{14}$$

with the return perid α denoted as:

$$\alpha = \frac{V_\alpha}{V_0}. \tag{15}$$

Complex components exhibit various HSVs whereas, mostly, each of them features differences in microstructure due to dependency on local casting process conditions. Thus, a local fatigue assessment considering the microstructural characteristics is beneficial. Even in case of the same microstructure, respectively basic defect distribution, the HSV depends on the component geometry and load condition, which lead to the question if single HSVs may be added together, resulting in a HSV of the whole part and fatigue strength design according to Equation (1), or if each HSV has to be considered individually for all unconnected ones. This paper clarifies this task regarding size effect based fatigue strength design in cast aluminium. Summing up, this paper scientifically contributes to the following points:

- The influence of disconnected highly-stressed volumes as statistical size effect based on accumulated highly-stressed volumes.

- The impact of the highly-stressed volume on the defect distribution and its associated parameters is verified for samples with not-yet investigated casting process conditions. This enhances the existing database and strengthens the a priori established model framework of probabilistic fatigue strength design.
- The effect of the element size during numerical evaluation of the highly-stressed volume is studied and supports recommendations for engineering applicability.
- The work validates the prior developed statistical size effect approach which depends not only on the return period of the highly-stressed volume but takes also the defect distribution of the fractograpic analysis and the material resistance as probabilistic values into account.

2. Investigated Alloy

The material is taken out of a gravity cast automotive part, manufactured using the core package system casting process [61,62]. The components are made of EN AC-46200 with T6 heat treatment [63], whose nominal chemical composition is given in Table 1. In general, applied steps for T6 heat treatment at aluminium alloys are solution treatment, quenching and age hardening, following defined temperature and time conditions [61,64,65]. First, solution treatment is conducted at high temperatures of approximately 490 °C to 510 °C for about 0.5 h to 8 h to dissolve Cu-rich particles [64–68]. The following quenching in water at ambient temperature, or at 60 °C, leads to a over-saturated solid solution [64,69]. In the third step, the age hardening process is conducted at temperatures from 160 °C to 210 °C for about 4 h to 18 h, whereat in case of higher temperatures a reduced time span is needed to reach the peak hardness, which is the overall aim of T6 treatment [64,67,70–74]. Furthermore, the peak hardness decreases with increasing age hardening temperature [64]. The specimens are manufactured from two different sampling positions, denoted as A and B, where A possesses a highly-stressed volume V_0 and B an increased highly-stressed volume V_1. Further information about these positions and its local microstructural and mechanical properties are given in detail in References [3,53,75,76]. Within these preliminary studies, the fundamental KTD was built up.

Table 1. Nominal chemical composition of the investigated cast alloy in weight percent [63].

Alloy	Si [%]	Cu [%]	Fe [%]	Mn [%]	Mg [%]	Ti [%]	Al [-]
EN AC-46200	7.5–8.5	2.0–3.5	0.8	0.15–0.65	0.05–0.55	0.25	balance

The secondary dendrite arm spacing (SDAS) in position A and B is almost identical and differ by only five percent, resulting in a negligible technological size effect between these two positions. The SDAS was evaluated through an automated procedure described in Reference [77] for linking the microstructural properties to quasi-static [78–80] and fatigue properties [7,73,81,82]. Thus, the chosen positions A and B feature specimens of varying geometric sizes but with almost identical microstructural and mechanical properties. The investigated samples possess the same basic circular cross section, but their total length differ. For clarification, specimen A is taken from position A and specimen B is manufactured out of position B. Subsequently, only the specimens are denoted as A and B. To reduce the stress concentration factor within the cross section transition region, the specimens have been numerically shape optimized resulting in a stress concentration factor of only 1.04.

The difference between specimen A and specimen B is, that in case of specimen B, the basic geometry of sample A has been invoked two times in a row. Thus, it is the same as two specimens of type A. Figures 2 and 3 depict the two specimen geometries for high cycle fatigue testing under uniaxial tension load.

The highly-stressed volume of specimen geometry B is roughly doubled in comparison to geometry A. Thus, considering the sum of both sections, a noticeable statistical size effect is expected. To determine the return period of the highly-stressed volumes more accurately, a numerical study regarding the applicable element seed is conducted. A linear elastic finite element analysis

has been set-up featuring an uni-axial tension load with couplings to match the experimental clamping conditions.

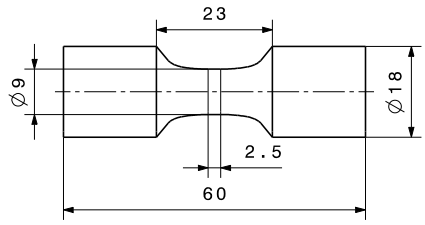

Figure 2. High cycle fatigue (HCF) specimen A with dimensions in [mm].

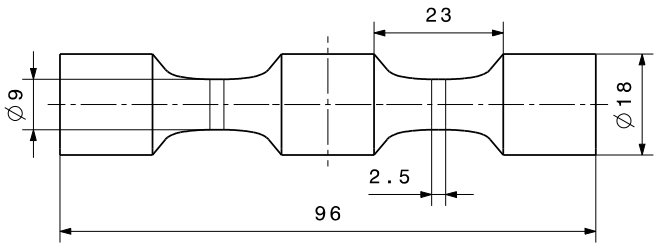

Figure 3. HCF specimen B with dimensions in [mm].

The element types employed are 20-node quadratic brick C3D20R and 10-node quadratic tetrahedron C3D10 elements with 8 up to 116 elements on each circumference. Additionally, axisymmetric CAX8R elements are used with the same element dimensions to significantly reduce the simulation time. This results in an average element size of approximately 0.24 mm to 3.5 mm in the HSV-region, see Figure 4. Another possibility to define the element seed, respectively number of elements per unit length, is the deviation factor, which is defined as the ratio between height h of the segment and the chord length L with n as element number on the circumference, see Equation (16).

$$\frac{h}{L} = \frac{1}{2} \cdot tan\left(\frac{\pi}{2 \cdot n}\right). \tag{16}$$

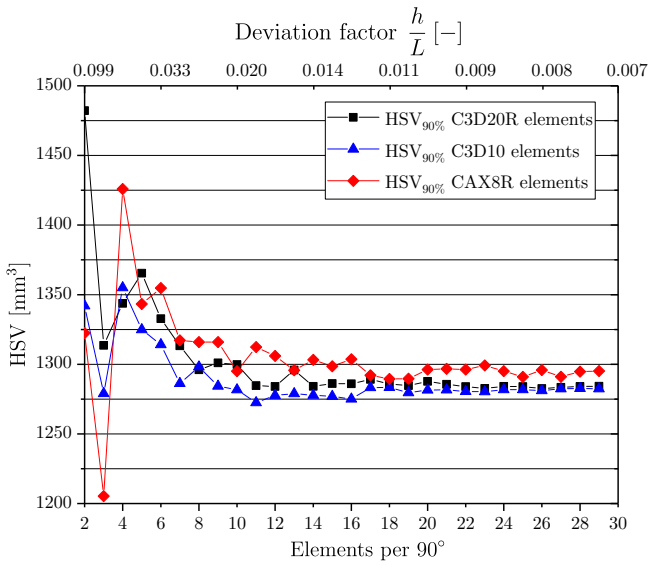

Figure 4. Effect of element seed on numerically determined highly-stressed volume (HSV).

Thus, a number of about 32 elements on circumference, or a deviation factor of 0.03, leads to a sound compromise between simulation time and accuracy. The numerically evaluated volume results

in a value of $V_{0,90\%} = 647$ mm^3 for specimen A and $V_{1,90\%} = 1284$ mm^3 for specimen B, see Figure 5. Concluding, a 90 % highly-stressed volume ratio of $\alpha = 1.98$ is obtained for specimen A and B.

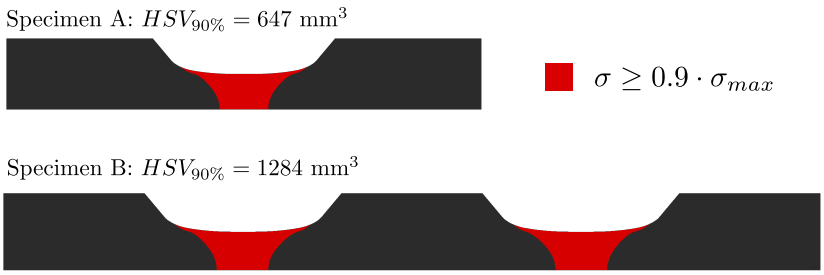

Figure 5. Finite Element (FE) analysis of specimens A and B with 90% HSV determined with C3D20R elements.

In the first phase of the testing procedure the experiment is carried out by clamping part 1 and 3 of the entire specimen with subsequent high cycle fatigue testing until rupture, either at the upper (section 2–3) or the lower (section 1–2) specimen fraction, as depicted in Figure 6. Next, the fractured part is removed (shorter specimen part of section 1 or section 3). Subsequently, the specimen is clamped at the middle part (section 2), see secondary clamping in Figure 6, and the test is continued at the same load level until rupture of the remaining short specimen. It should be highlighted that this shortened specimen possess a HSV which is equivalent to specimen geometry A. The result of this testing procedure are two points in the S/N diagram, which will be discussed in more detail in Section 3.

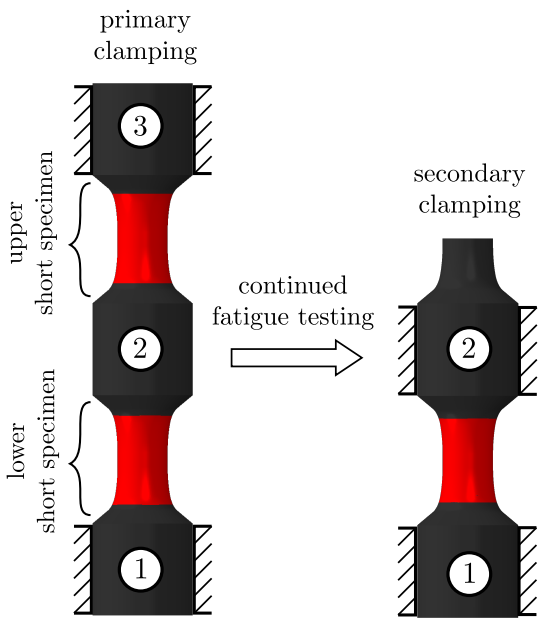

Figure 6. First and second testing of specimen type B.

In order to ensure a homogeneously distributed surface quality with prevention of human influence by polishing, the specimens are polished by a vibratory finishing process. After the CNC machining process, the components are placed in an oscillating bowl containing polishing media. Thereby, the specimens are precision grinded and polished with different abrasive media for several hours until the required surface quality is obtained.

3. Experimental Results

3.1. Fatigue Strength

The fatigue strength of the material is determined at a resonant testing machine with a testing frequency of about 108 Hz with compression/tension loading at a stress ratio of R = −1. In order to focus on the long life fatigue region, the run-out number was set to ten million load cycles. Previous investigations [3] indicated that the transition knee point is close to about two million load cycles for such unnotched samples made of aluminium alloy. As proposed in Reference [83] and applied in preliminary studies [3,76,83,84], the slope of the S/N-curve in the long life region k_2 scales with the slope in the finite life region k_1 and therefore it is assigned with $k_2 = 5 \cdot k_1$. The S/N curve in the finite life region is evaluated by the statistical procedure given in the standard [85]. The long life region is assessed by the $arcsin\sqrt{P}$ methodology, as proposed in Reference [86]. In the following, the long life fatigue strength of specimen A, taken out of position A, at ten million load cycles and at a probability of survival $P_S = 50$ % is used as unifying reference value. Figure 7 presents the statistically evaluated S/N curve of specimen A series including the 90% and 10% scatter band. Be aware that specimen A inherit the highly-stressed volume V_0.

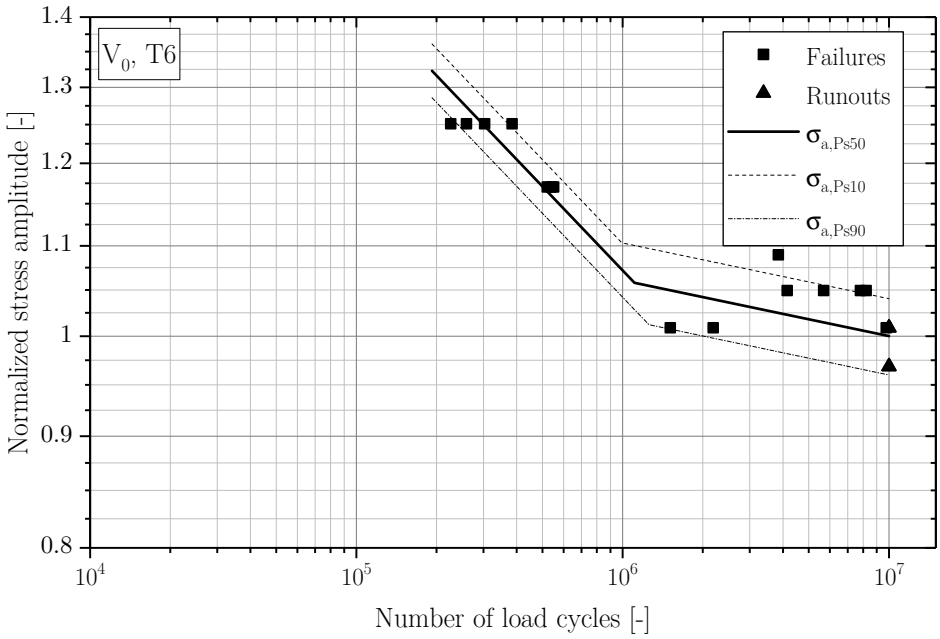

Figure 7. S/N curve of specimen A.

Next, the evaluated fatigue data of specimen B at first failure is depicted in Figure 8, again with the 90% and 10% scatter band of the high cycle fatigue region. Thus, the mean long-life fatigue strength σ_{LLF} of position B decreased by approximately five percent compared to specimen A. The doubling of the highly-stressed volume in position B reveals an evaluable decrease in fatigue strength contributed as statistical size effect.

The evaluated slope k_1 at position B in the finite life region is somewhat higher with respect to position A. Additionally, the number of load cycles N_T of the transition knee-point is slightly enhanced. Comparing the scatter indices T_S of the positions A and B, an increase at disconnected highly-stressed volumes is observed. The evaluated long life fatigue strength σ_{LLF} is listed in Table 2, where all fatigue strengths are normalized by position A with a probability of survival $Ps = 50$ %. Furthermore, the slope k_1 of the finite life region, the number of load cycles for the transition knee-point N_T and the statistically evaluated fatigue scatter index T_S are given in Table 2.

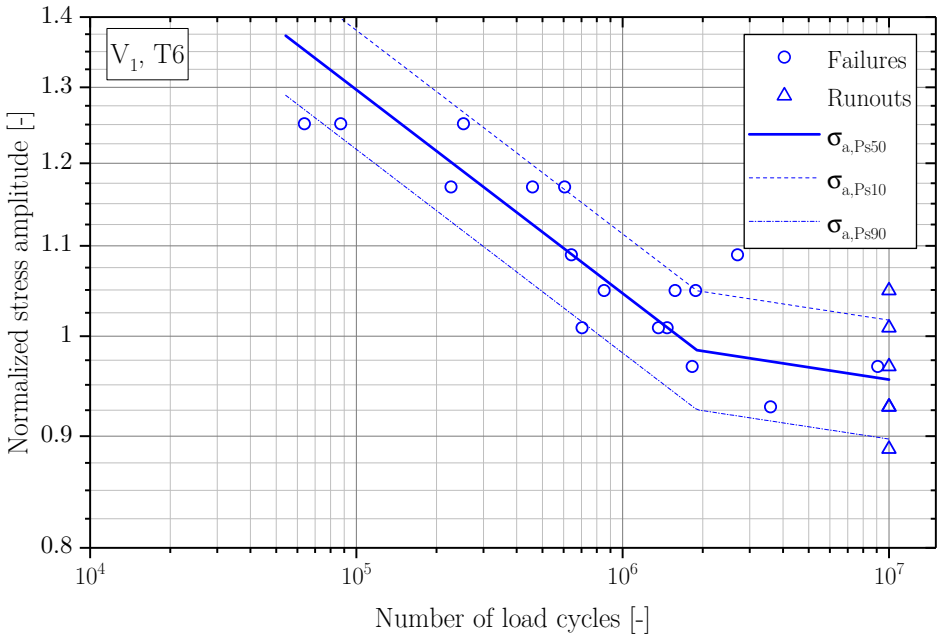

Figure 8. S/N curve of specimen B (evaluation only first failures).

Table 2. Results of the fatigue tests of specimen A and B.

Specimen	HT	Volume	k_1 [-]	$\sigma_{LLF,50\%}$ [-]	N_T [-]	T_S [-]
A	T6	V_0	7.84	1.00	1,100,000	1:1.08
B	T6	V_1	10.73	0.96	1,900,000	1:1.23

Thus, the statistical size effect may be clearly identified for such samples possessing an increased highly-stressed volume, even though this volume is not coherent as shown in Figure 5. On the other hand, if the highly-stressed volume would be considered separately, which means that no statistical size effect occurs in case of non-coherent highly-stressed volume, both S/N curves in Figures 7 and 8 must coincide. Therefore, the experimental point $\sigma_{B,Ps50}$ should be congruent with the point $\sigma_{A,Ps50}$ for the same connected highly-stressed volume. But the experimental point of specimen B (V_1) with two separated highly-stressed volumes V_0 is below the fatigue strength of specimen A (V_0).

Therefore, as main finding based on the presented experiments, the entire highly-stressed volume has to be considered for the statistical size effect. Thereby, the entire highly-stressed volume V_1 is calculated by the sum of the separated, non-coherent highly-stressed volumes whereat the failure of one single highly-stressed volume leads to a collapse of the specimen. The working hypothesis for first, and second, fatigue failure of specimen B and a theoretical discussion is given in detail in Appendix A.

3.2. Fractography

The crack initiating defect sizes of the HCF specimens are evaluated subsequently to the fatigue testing utilizing a digital optical microscopy for macroscopic inspection and scanning electron microscopy respectively for magnification enhanced, local analysis. According to previous investigations [5,53], defect sizes are evaluated by their precise contour in contrast to the coarser method proposed by Murakami in Reference [59], where a smooth hull contour, which envelopes the original shape, is utilized. This measurement methodology leads to smaller, but more precisely evaluated defect sizes, and it minimizes the distortive effects of projected pore shape onto the statistical evaluation of defect sizes. Therefore, a spline is drawn manually at the contour of the defect using the software Fiji, allowing to calculate the enclosed area. The analysis of the initiating cracks of the specimen A and B revealed that in most cases the technical crack initiates at surface near defects, as depicted in Figure 9. Thus, the increased stress intensity of surface-intersecting defects and surface near

defects lead to a lowered crack initiation phase compared to closed defects within the bulk volume [53]. With the existence of superior internal defects in a few samples, in the majority of them specimen B cases, origin of fracture is shifted into the centre of the specimen, exemplary see Figure 10.

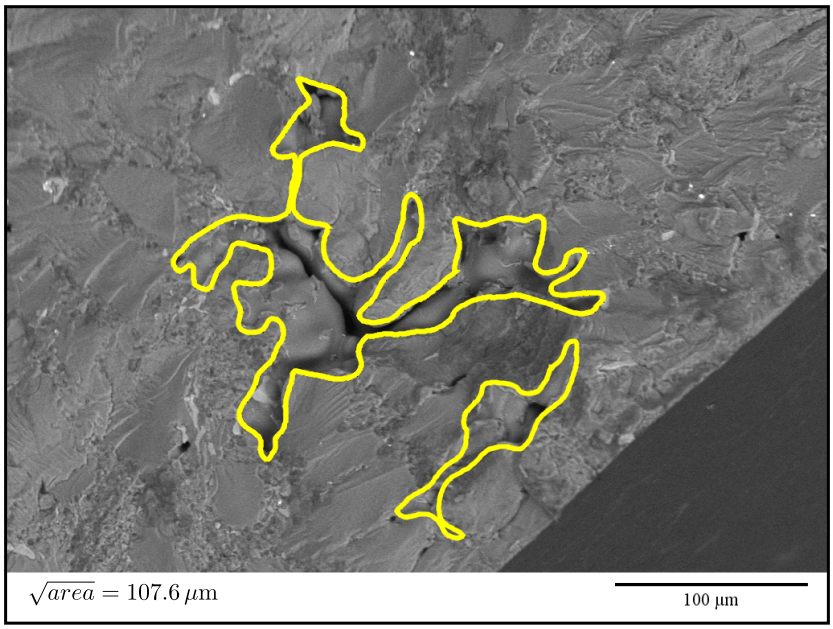

Figure 9. Fracture initiating defect at specimen A.

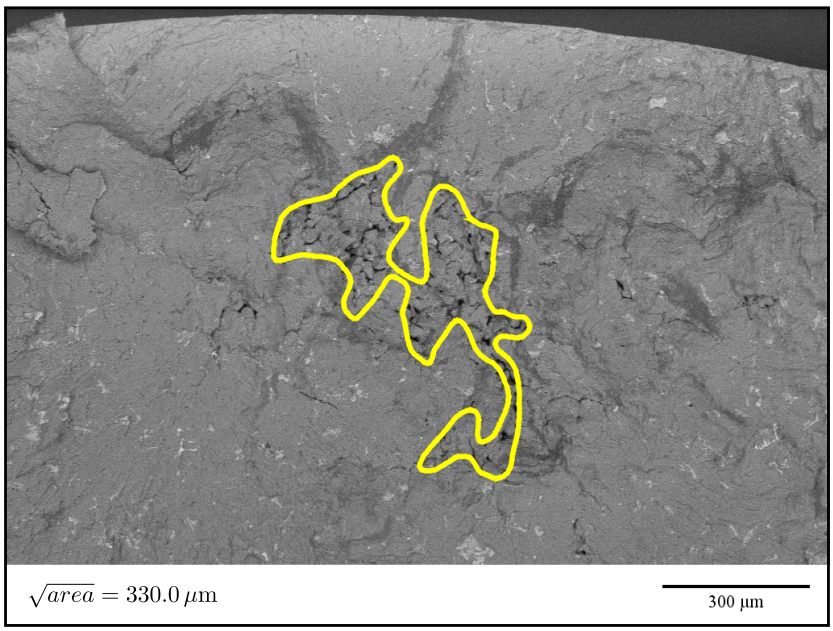

Figure 10. Fracture initiating defect at specimen B.

As depicted in Figure 11, in a few cases another failure mechanism is recognizable. According to previous studies [5,87] large slip plane areas can operate as failure reason for load amplitudes within the finite life region. This is more likely to happen for increasing loads. It is stated in References [88,89], that in fine microstructures with a small SDAS, the dislocations are able to move across the cell boundaries of the dendrites, since there are no particles to block them. This is in contrast to larger SDAS values by means of coarse microstructures where the dendrite cell is isolated by a thick eutectic wall blocking the dislocations. Due to that, a critical defect size exists, below that the crack initiates at slip bands instead of interdendritic shrinkage pores. From preliminary studies [5,53] it can be assumed

that this failure mechanism only occurs at specimens with lower SDAS and quite high load levels of the S/N-curve.

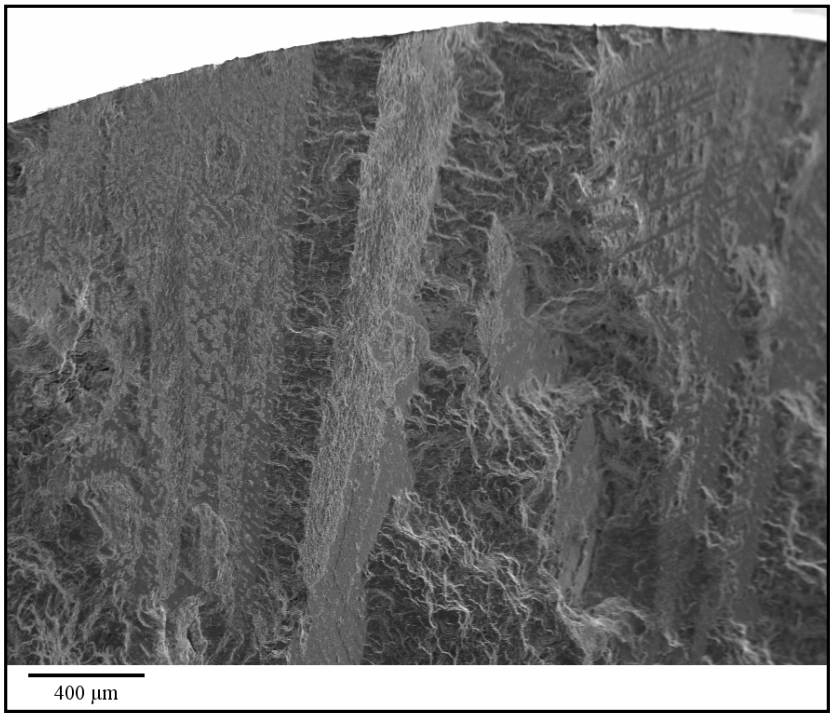

Figure 11. Slip plane area that occurs in both positions.

Summing up the experimental work, the fractographic analysis revealed that in most cases the crack initiation starts at interacting shrinkage porosity near the surface, see Figure 9. Therefore, defects are regarded as interacting if the distance between two defects is less than the size of the smaller defect, as proposed in Reference [90]. For the subsequent statistical evaluation of the critical defect sizes the generalized extreme value distribution is applied, following the proposal of Reference [13]. The associated cumulative distribution function (CDF) is given in Equation (6). Following Reference [91], a Kolmogorov-Smirnov (KS) test is conducted to evaluate the goodness of fit for the statistical assessment of the distribution. A perfect compliance for the fit is given with a value of $p_{KS} = 1.00$ in the KS-test.

The evaluated probability of occurrence P_{Occ} of casting defects for the reference volume V_0 as well as the two times enlarged volume V_1, reflecting specimen A and B, is drawn in Figure 12. Assuming that the failure of one section causes the failure of the whole component, only the first fracture and its associated flaw size are utilized for the evaluation of the distribution parameters. In addition, the parameters for the distributions in Figure 12 are statistically evaluated using the maximum likelihood estimation, as proposed in Reference [56]. The evaluated parameters of the distributions from specimen A and B, the result of the Kolmogorov-Smirnov test and the evaluated defect size with a probability of occurrence of 50% are listed for comparison in Table 3.

Table 3. Statistically evaluated distribution parameters of the generalized extreme value distribution (GEV).

Position	Volume	μ [µm]	δ [µm]	ξ [-]	$\sqrt{area}(P_{Occ=0.5})$ [µm]	p_{ks} [-]
A	V_0	95.1	20.1	0.43	103	0.93
B	V_1	118.4	28.1	0.36	129	0.69
B (model)	V_1	111.3	27.1	0.43	122	0.58

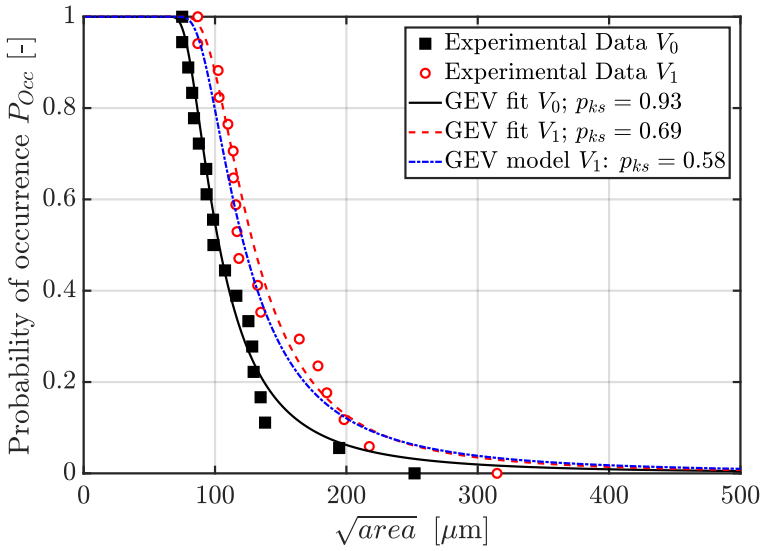

Figure 12. Probability of occurrence of critical defect sizes in specimen A and B.

As mentioned before, in this study only the first failures per specimen are considered for the validation of the statistical size effect. The probability of occurrence P_{Occ} of a critical defect for an α-times enlarged volume V_α can be estimated based on the statistical distribution of the reference volume as reasoned in Reference [3] and shown in Equation (17). The evaluation of the location μ_α, shape ξ_α and scale δ_α parameter for the distribution P^α is given in Equations (8)–(10). The parameters of the distribution P^α are listed in Table 3.

$$P^\alpha = \exp\left\{-\left[1+\xi_\alpha\left(\frac{\sqrt{area}-\mu_\alpha}{\delta_\alpha}\right)\right]^{-\frac{1}{\xi_\alpha}}\right\}. \tag{17}$$

4. Verification of Size-Effect Related Fatigue Strength

In order to study the size effect as influence of the highly stressed volume, the probabilistic model of the preliminary work [3] has to be applied to evaluate the local Weibull factor κ. It depends on the return period α of the highly-stressed volume and the local defect population μ_0. As the same aluminium alloy with T6 heat treatment was used also in the previous model development regarding fatigue strengths, the diagram can be easily rebuilt for the varying return period, respective defect population within the highly-stressed volume. The local Weibull factor $\kappa(\mu_0, \alpha)$ can be obtained by transforming Equation (1). This results in a value of $\kappa_{\mu_0,\alpha} = 15.27$ based on the experimental results for the α-times enlarged volume in case of specimen B, see Equation (18).

$$\kappa(\mu_0, \alpha) = \frac{\log(\alpha)}{\log(\Delta\sigma_{\mathrm{LLF},V_0}) - \log(\Delta\sigma_{\mathrm{LLF},V_\alpha})}. \tag{18}$$

In the fundamental work of Reference [3], the Kitagawa-Takahashi diagram (KTD) was used to assess the fatigue strength $\Delta\sigma_{\mathrm{LLF},V_0}$ and $\Delta\sigma_{\mathrm{LLF},V_\alpha}$ depending on defects, respective microcracks. Therein, crack propagation tests have been conducted with specimens manufactured from the identical positions as used in this study to minimize microstructural deviations. To extend the KTD for physically short and long cracks, the crack-resistance curve was implemented [4]. A summary of the fracture mechanical variables, determined by crack propagation tests from previous studies [4], is given in Table 4 for the investigated alloy. No statistically feasible difference in fracture mechanical material properties of position A and B has emerged.

Table 4. Parameters resulting from crack propagation tests in position A and B for a probability of occurrence of $P_{Occ} = 50\%$.

$\Delta K_{th,lc}$ [MPa$\sqrt{\text{m}}$]	$\Delta K_{th,eff}$ [MPa$\sqrt{\text{m}}$]	ν_1 [-]	ν_2 [-]	l_1 [mm]	l_2 [mm]
3.95	1.06	0.4	0.6	0.03	0.75

The long life fatigue strength of the near defect free material $\Delta\sigma_0$, which defines the upper limit of the left side of the KTD, was evaluated with specimens in HIP treatment condition at the same position. In this model the fatigue strength $\Delta\sigma_{LLF,V_0}$ is determined using the R-curve extension [40] for a defect size represented by the size of an defect a_m of the reference volume V_0 implying a probability of occurrence of $P_{Occ} = 50\%$. The critical defect size for an enhanced volume can be estimated by application of Equations (6)–(12). This results in a fatigue strength $\Delta\sigma_{LLF,V\alpha}$ for an enhanced volume V_α using the given defect distribution (μ_α,δ_α) with a specific defect size $a_{m,\alpha}$.

$$\Delta\sigma_{\text{LLF},V_0} = \frac{\Delta K_{th,\Delta a}}{Y \cdot \sqrt{\pi \cdot a_m}}, \tag{19}$$

with

$$\Delta K_{th,\Delta a} = \Delta K_{th,eff} + \left(\Delta K_{th,lc} - \Delta K_{th,eff}\right)\left[1 - \sum_{i=0}^{n} \nu_i \cdot \exp\left(-\frac{\Delta a}{l_i}\right)\right], \tag{20}$$

$$a_m = \mu_0 + \delta_0\left(-log(-log(P))\right), \tag{21}$$

$$\Delta a = a_m - a_{0,eff}, \tag{22}$$

$$a_{0,eff} = \frac{\Delta K_{th,eff}}{(Y \cdot \Delta\sigma_0)^2} \cdot \frac{1}{\pi}. \tag{23}$$

Thus, the long life fatigue strength of the reference volume V_0 with a certain defect distribution can be calculated using Equations (19)–(23). Moreover, the fatigue strength of an enlarged volume V_α can be determined by means of Equation (24) to (27), (20) and (23), as exemplified in Reference [3].

$$\Delta\sigma_{\text{LLF},V_\alpha} = \frac{\Delta K_{th,\Delta a}}{Y \cdot \sqrt{\pi \cdot a_{m,\alpha}}}, \tag{24}$$

with

$$a_{m,\alpha} = \mu_\alpha + \delta_\alpha\left(-log(-log(P))\right), \tag{25}$$

$$\Delta a = a_{m,\alpha} - a_{0,eff}, \tag{26}$$

$$\mu_\alpha = \mu_0 + log(\alpha) \cdot \delta_0, \tag{27}$$

$$\delta_\alpha = \delta_0. \tag{28}$$

Now, the local Weibull factor $\kappa(\mu_0, \alpha)$ can be derived as a function of inhomogeneity population represented by its location parameter μ_0 in a control volume V_α. The course of the local Weibull factor κ is plotted in dependence of α and μ_0 in Figure 13. It is evident that κ increases with rising return period α and defect population μ_0. This relationship is a significant improvement compared to the common guideline [23], where the Weibull factor is determined with a constant value of ten.

Hence, this generalized model of Aigner et al. [3] can be used to check on the size effect of the return period α, thereby validating the influence of disconnected highly-stressed volumes, as discussed in Section 3.2. Therefore the evaluated defect distribution for the reference volume V_0 in Section 3.2 and the return period of $\alpha = 1.98$ are utilized and leading to a model-based local Weibull factor of $\kappa(\mu, \alpha) = 13.8$, as depicted in Figure 13 as red marked triangle.

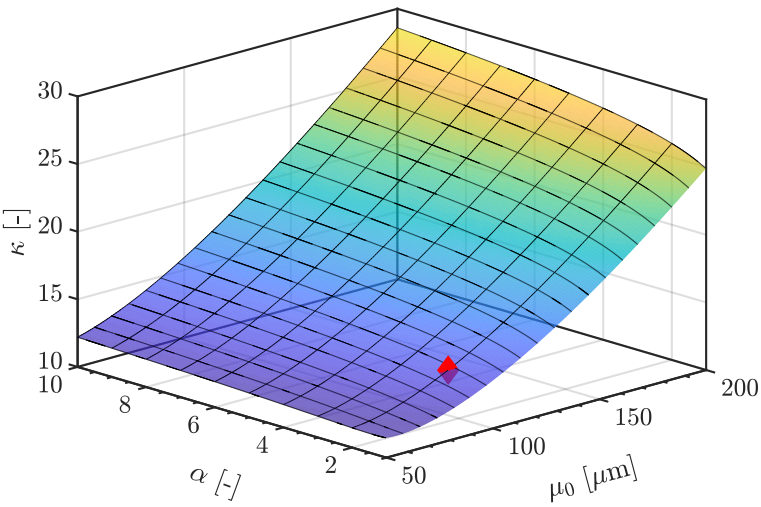

Figure 13. Weibull factor κ depending on the return period α and the defect population μ_0 and evaluated point of the current test series of specimen B.

By applying the common guideline [23], respectively, the volumetric model of Sonsino [16], (Equation (1)), the fatigue strength of an elevated HSV with return period α, defined as V_α, can be calculated as a function of a reference volume V_0 and its associated parameters. The calculation is done for the HSV of specimen B.

Aside from the discussed volumetric approaches, the estimation of the Weibull factor can be related to the scatter index of the experimental fatigue strength distribution only [17], see Equation (2). Substantiated by the high manufacturing quality of the samples and quite homogeneous manufacturing process conditions within the HSV, a comparably small fatigue scatter index T_S in the long-life fatigue region is obtained. This approach leads to a value of $\kappa = 39.3$, resulting in non-conservative fatigue data. This is depicted as dash-dotted line in Figure 14.

In Figure 14, all three different approaches [3,17,23] are compared, where each of them leads to different Weibull factors κ resulting in differing fatigue strength values. Table 5 lists the normalized fatigue strength results from the three different κ-values. The fatigue assessment model proposed in Reference [3] fits the experimental data with a value of $\kappa = 13.8$ best, plotted as continuous line in Figure 14. The common guideline (dotted line in Figure 14) leads to a more conservative fatigue design compared to the experimental results, because a constant weibull factor κ is defined for groups of materials. The model published by Reference [17] leads to an improper, non-conservative fatigue design due to the small scatter band of the fatigue data.

Table 5. Comparison of the normalized fatigue strength resulting from different Weibull parameters κ using a return period of $\alpha = 1.98$ (specimen B in this study).

$\sigma_{LLF,50\%}$ [-]	Δ	κ [-]	Model
0.96	Reference	-	Experiment
0.93	−2.28%	10.0	[23]
0.98	+2.84%	39.3	[17]
0.95	−0.42%	13.8	[3]

To summarize, the fatigue assessment model of Reference [3] is validated for EN AC-46200 in sand cast condition for volume ratios up to a value of α about two, leading to an enhanced fatigue assessment avoiding an over-conservative design. The updated size effect model, utilizing a highly stressed volume of 90%, now covers a return period of about two and up to six [3]. Nevertheless, other return periods shall be investigated to approve the statistical method even further.

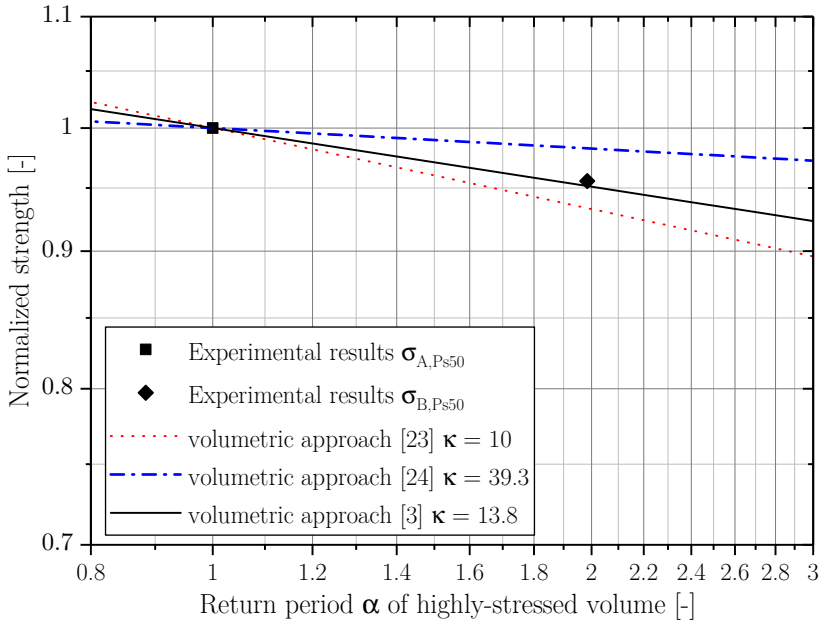

Figure 14. Comparison of HSV-based fatigue assessment models for S/N-results of specimen A and B.

5. Conclusions

This paper evaluates the size-effect based fatigue strength design of EN AC-46200 in T6 heat treatment condition. Therefore, a special specimen geometry was designed, which possess a non-coherent highly-stressed volume. Volumetric approaches are reviewed and their applicability for conservative fatigue designs is discussed. Overall, the following conclusions can be drawn:

- Based on a numerical parameter study, a deviation factor of about 0.03 is recommendable for numerical evaluation of the highly-stressed volume (HSV) in engineering applications.
- If several independent HSVs with the same microstructural properties are attached as one component and loaded simultaneously, the failure of each HSV leads to failure of the whole component. Hence, the aggregated sum of disconnected HSVs has to be considered as size effect in fatigue strength design. But in the case of varying microstructures between the individual highly-stressed volumes, the local microstructure has to be considered as well.
- The conducted validation of the aforesaid defect based probabilistic fatigue assessment model, originally published in Reference [3], is based on samples with a return period of about two. The results confirm that the model assesses the fatigue strength in terms of statistical size effect best by applying the local Weibull factor κ depending on the return period α and defect population μ_0. Thus, the verified probabilistic approach is recommendable for engineering design of complex parts, whereat the HSV has to be linked to the local microstructural properties for proper fatigue strength design.

Current work focuses on the design strength related interaction between HSV and associated microstructure in cast aluminium alloys, especially in case of service load cases which enforces locally varying HSV and subsequent feasible damage sum calculations. Moreover, the applicability of the design concept for notched components considering different load cases and local stress gradients will be investigated.

Author Contributions: Conceptualization, M.O., S.P., M.L. and M.S.; methodology, M.O., S.P. and M.S.; software, M.O., M.S. and S.P.; validation, M.O. and M.L.; formal analysis, M.O. and S.P.; investigation, M.O.; resources, M.S.; data curation, M.O.; writing–original draft preparation, M.O.; writing–review and editing, M.O., M.L., S.P. and M.S.; visualization, M.O.; supervision, M.L. and M.S.; project administration, M.S.; funding acquisition, M.S.; All authors have read and agreed to the published version of the manuscript.

Funding: This research was funded by the Austrian Federal Ministry for Digital and Economic Affairs and the National Foundation for Research, Technology and Development.

Acknowledgments: The financial support by the Austrian Federal Ministry for Digital and Economic Affairs and the National Foundation for Research, Technology and Development is gratefully acknowledged. Furthermore, the authors would like to thank the industrial partners BMW AG and Nemak Dillingen GmbH for the excellent mutual scientific cooperation within the CD-laboratory framework.

Conflicts of Interest: The authors declare no conflict of interest.

Abbreviations

The following abbreviations are used in this manuscript:

$\sqrt{area}$	Defect size of Murakami's approach
α	Return period of the highly-stressed volume
κ	Weibull factor
σ_{LLF}	Long life fatigue strength
σ_{LLF,V_0}	Long life fatigue strength of the reference volume V_0
σ_{LLF,V_α}	Long life fatigue strength of the α-times enlarged volume V_α
$\sigma_{LLF,50}$	Estimated long life fatigue strength with 50% probability of survival
$\sigma_{*,Ps50}$	Experimental long life fatigue strength at position * with 50% probability of survival
Δ	Deviation of model to experiment
$\Delta\sigma_0$	Fatigue range of near defect free material
δ	Scale parameter of the GEV distribution
δ_0	Scale parameter of the GEV distribution for the reference volume V_0
δ_α	Scale parameter of the GEV distribution for the α-times enlarged volume V_α
μ	Location parameter of the GEV distribution
μ_0	Location parameter of the GEV distribution for the reference volume V_0
μ_α	Location parameter of the GEV distribution for the α-times enlarged volume V_α
ξ	Shape parameter of the GEV distribution
ξ_α	Shape parameter of the GEV distribution for the α-times enlarged volume V_α
ν_i	Weighting factor for crack closure effect i
l_i	Crack elongation, where the crack closure effect ν_i is completely build-up
$\Delta K_{th,lc}$	Long crack threshold range
$\Delta K_{th,\Delta a}$	Crack threshold range in respect to the crack extension
$\Delta K_{th,eff}$	Effective crack threshold range
ΔK_{eff}	Effective stress intensity factor range
K_{max}	Maximum stress intensity factor
K_{op}	Opening stress intensity factor
Δa	Crack extension
a	Crack length
$a_{0,eff}$	Intrinsic crack length
$a_{0,lc}$	Crack length at the transition to long crack behaviour
a_m	Crack length of the reference volume V_0 for a probability of occurrence of 50%
$a_{m,\alpha}$	Crack length of the reference volume V_α for a probability of occurrence of 50%
h	Segment height of a circle
L	Chord length of the segment
n	Number of elements on circumference
P	Probability
P_{Occ}	Probability of occurrence
P_S	Probability of survival
P^α	Defect distribution of α-times enlarged volume V_α
V_0,V_1	Highly stressed volume of specimen A and B
$V_{90,0}$,$V_{90,1}$	90% highly stressed volume of specimen A (V_0) and B (V_1)
V_∞	Threshold volume

V_α	α-times enlarged highly stressed volume
p_{ks}	p-value of the Kolmogorov-Smirnov test
Y	Geometry factor
k_1	Inverse slope of the S/N-curve in finite life region
k_2	Inverse slope of the S/N-curve in long life region
T_S	Fatigue scatter band of the S/N-curve
N_T	Transition knee point of the S/N-curve
R	Load ratio
R-curve	Cyclic crack resistance curve
HSV	Highly stressed volume
SDAS	Secondary dendrite arm spacing
GEV	Generalized extreme value distribution
CDF	Cumulative distribution function
KTD	Kitagawa Takahashi diagram
ECD	Equivalent circle diameter
FE	Finite element
HCF	High cycle fatigue
HIP	Hot isostatic pressing

Appendix A. Fatigue Failure Hypothesis

Lets assume that there is a cube containing a homogeneous defect distribution. Therefore, specimens manufactured from this cube, containing a certain highly stressed volume V_0, named specimen geometry A in this hypothesis, see Figure A1. This homogeneous distribution of defects results in a fatigue strength σ_{LLF,V_0}, inheriting a defect distribution GEV_{V_0}, evaluated by means of a fractographic analysis. Next, specimens possessing a connected doubled highly-stressed volume V_1 are manufactured from the same cube, which results in a fatigue strength σ_{LLF,V_1} with associated defect distribution GEV_{V_1}. According to [3], this defect distribution GEV_{V_1} is shifted to larger defect sizes compared to the GEV_{V_0} caused by the increased probability for larger, extremal defects in an increased highly-stressed volume. In the third step, two cubes containing a highly stressed volume V_0 are linked together as specimen B, to get a disconnected highly-stressed volume, which is two times V_0, see Figure 3. This results also in a lowered fatigue strength σ_{LLF,V_1} considering only the first failure of each specimen.

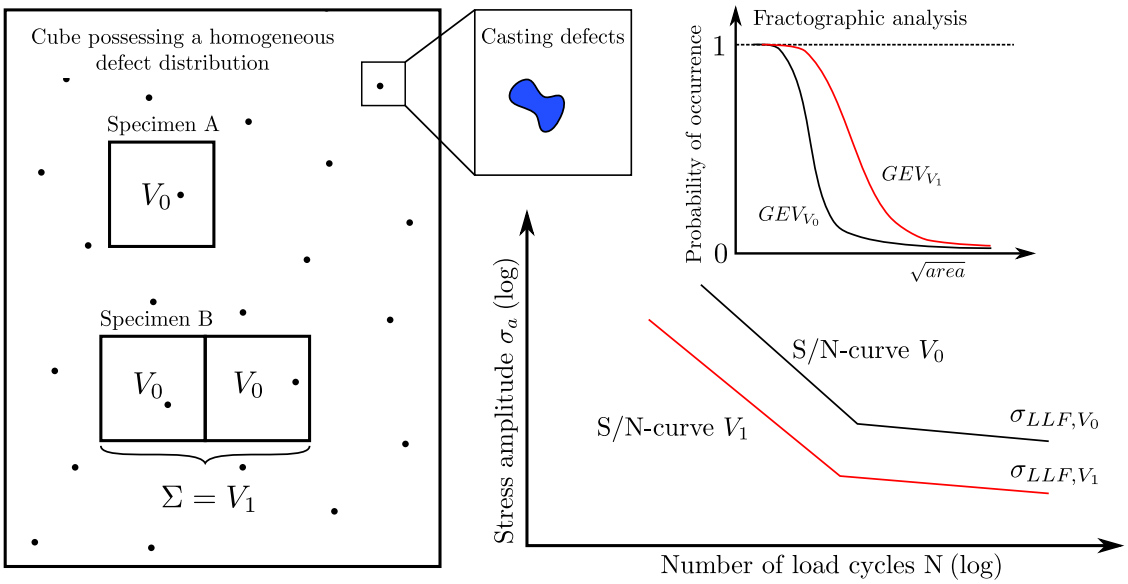

Figure A1. Schematic representation of the specimens manufactured from a cube possessing a homogeneous defect distribution and sketch of expected fatigue strength results.

Additionally, the fatigue strength of the second failures should result towards the higher value σ_{LLF,V_0}. Considering the defect distributions in the third case, the fractographical evaluated defect distribution of the first failures is supposed to coincide with GEV_{V_1} and the defect distribution of the second failures should coincide with GEV_{V_0}.

References

1. Hertel, O.; Vormwald, M. Statistical and geometrical size effects in notched members based on weakest-link and short-crack modelling. *Eng. Fract. Mech.* **2012**, *95*, 72–83, doi:10.1016/j.engfracmech.2011.10.017. [CrossRef]
2. Tomaszewski, T.; Sempruch, J. Size effect in high-cycle fatigue. *J. Mach. Constr. Maint. Probl. Eksploat.* **2017**, *1*, 29–35.
3. Aigner, R.; Pomberger, S.; Leitner, M.; Stoschka, M. On the Statistical Size Effect of Cast Aluminium. *Materials* **2019**, *12*, 1578, doi:10.3390/ma12101578. [CrossRef]
4. Aigner, R.; Pusterhofer, S.; Pomberger, S.; Leitner, M.; Stoschka, M. A probabilistic Kitagawa-Takahashi diagram for fatigue strength assessment of cast aluminium alloys. *Mater. Sci. Eng. A* **2019**, *745*, 326–334, doi:10.1016/j.msea.2018.12.108. [CrossRef]
5. Aigner, R.; Leitner, M.; Stoschka, M. Fatigue strength characterization of Al-Si cast material incorporating statistical size effect. In Proceedings of the MATEC Web Conference, Poitiers, France, 27 May—1 June 2018; Volume 165, p. 14002. [CrossRef]
6. Yi, J.Z.; Gao, Y.X.; Lee, P.D.; Lindley, T.C. Microstructure-based fatigue life prediction for cast A356-T6 aluminum-silicon alloys. *Metall. Mater. Trans. B* **2006**, *37*, 301–311. [CrossRef]
7. Iben Houria, M.; Nadot, Y.; Fathallah, R.; Roy, M.; Maijer, D.M. Influence of casting defect and SDAS on the multiaxial fatigue behaviour of A356-T6 alloy including mean stress effect. *Int. J. Fatigue* **2015**, *80*, 90–102, doi:10.1016/j.ijfatigue.2015.05.012. [CrossRef]
8. Stroppe, H. Calculation of the S-N curve for cast aluminium alloys based on static tensile test and dendrite arm spacing: Berechnung der Wöhler–Linie für Aluminium–Gusslegierungen aus dem statischen Zugversuch und dem Dendritenarmabstand. *Mater. Werkst.* **2009**, *40*, 738–742. [CrossRef]
9. Brueckner-Foit, A.; Luetje, M.; Wicke, M.; Bacaicoa, I.; Geisert, A.; Fehlbier, M. On the role of internal defects in the fatigue damage process of a cast Al-Si-Cu alloy. *Int. J. Fatigue* **2018**, *116*, 562–571, doi:10.1016/j.ijfatigue.2018.07.012. [CrossRef]
10. Brueckner-Foit, A.; Luetje, M.; Bacaicoa, I.; Geisert, A.; Fehlbier, M. On the role of internal defects in the fatigue damage process of a cast Al-Si-Cu alloy. *Procedia Struct. Integr.* **2017**, *7*, 36–43, doi:10.1016/j.prostr.2017.11.058. [CrossRef]
11. Atxaga, G.; Pelayo, A.; Irisarri, A.M. Effect of microstructure on fatigue behaviour of cast Al–7Si–Mg alloy. *Mater. Sci. Technol.* **2013**, *17*, 446–450, doi:10.1179/026708301101510023. [CrossRef]
12. Tiryakioğlu, M. On the size distribution of fracture-initiating defects in Al- and Mg-alloy castings. *Mater. Sci. Eng. A* **2008**, *476*, 174–177, doi:10.1016/j.msea.2007.04.088. [CrossRef]
13. Tiryakioğlu, M. Statistical distributions for the size of fatigue-initiating defects in Al–7%Si–0.3%Mg alloy castings: A comparative study. *Mater. Sci. Eng. A* **2008**, *497*, 119–125, doi:10.1016/j.msea.2008.06.023. [CrossRef]
14. Anderson, K.V.; Daniewicz, S.R. Statistical analysis of the influence of defects on fatigue life using a Gumbel distribution. *Int. J. Fatigue* **2018**, *112*, 78–83, doi:10.1016/j.ijfatigue.2018.03.008. [CrossRef]
15. Kuguel, R. A relation between theoretical stress concentration factor and fatigue notch factor deduced from the concept of highly stressed volume. *Proc. ASTM* **1961**, *61*, 732–748.
16. Sonsino, C.M. Zur Bewertung des Schwingfestigkeitsverhaltens von Bauteilen mit Hilfe örtlicher Beanspruchungen. *Konstruktion* **1993**, *45*, 25–33.
17. Diemar, A.; Thumser, R.; Bergmann, J.W. Statistischer Größeneinfluss und Bauteilfestigkeit. *Mater. Test.* **2004**, *46*, 16–21.
18. Böhm, J.; Heckel, K. Die Vorhersage der Dauerschwingfestigkeit unter Berücksichtigung des statistischen Größeneinflusses. *Mater. Werkst.* **1982**, *13*, 120–128, doi:10.1002/mawe.19820130408. [CrossRef]

19. Kuwazuru, O.; Murata, Y.; Hangai, Y.; Utsunomiya, T.; Kithara, S.; Yoshikawa, N. X-Ray CT Inspection for Porosities and Its Effect on Fatigue of Die Cast Aluminium Alloy. *J. Solid Mech. Mater. Eng.* **2008**, *2*, 1220–1231, doi:10.1299/jmmp.2.1220. [CrossRef]
20. Rotella, A.; Nadot, Y.; Piellard, M.; Augustin, R.; Fleuriot, M. Fatigue limit of a cast Al-Si-Mg alloy (A357-T6) with natural casting shrinkages using ASTM standard X-ray inspection. *Int. J. Fatigue* **2018**, *114*, 177–188, doi:10.1016/j.ijfatigue.2018.05.026. [CrossRef]
21. González, R.; González, A.; Talamantes-Silva, J.; Valtierra, S.; Mercado-Solís, R.D.; Garza-Montes-de Oca, N.F.; Colás, R. Fatigue of an aluminium cast alloy used in the manufacture of automotive engine blocks. *Int. J. Fatigue* **2013**, *54*, 118–126, doi:10.1016/j.ijfatigue.2013.03.018. [CrossRef]
22. González, R.; Martínez, D.I.; González, J.A.; Talamantes, J.; Valtierra, S.; Colás, R. Experimental investigation for fatigue strength of a cast aluminium alloy. *Int. J. Fatigue* **2011**, *33*, 273–278, doi:10.1016/j.ijfatigue.2010.09.002. [CrossRef]
23. *Rechnerischer Festigkeitsnachweis für Maschinenbauteile aus Stahl, Eisenguss- und Aluminiumwerkstoffen*, 6th ed.; FKM-Richtlinie, VDMA-Verl.: Frankfurt am Main, Germany, 2012; Volume 6.
24. Sonsino, C.M.; Ziese, J. Fatigue strength and applications of cast aluminium alloys with different degrees of porosity. *Int. J. Fatigue* **1993**, *15*, 75–84, doi:10.1016/0142-1123(93)90001-7. [CrossRef]
25. Weibull, W. Zur Abhängigkeit der Festigkeit von der Probengröße. *Ingenieur-Archiv* **1959**, *28*, 360–362. [CrossRef]
26. Gänser, H.P. Some notes on gradient, volumetric and weakest link concepts in fatigue. *Comput. Mater. Sci.* **2008**, *44*, 230–239, doi:10.1016/j.commatsci.2008.03.021. [CrossRef]
27. Abroug, F.; Pessard, E.; Germain, G.; Morel, F.; Hénaff, G. Fatigue size effect due to defects in an AA7050 alloy. In Proceedings of the MATEC Web Conference, Poitiers, France, 27 May—1 June 2018; Volume 165, p. 14015. [CrossRef]
28. Abroug, F.; Pessard, E.; Germain, G.; Morel, F. A probabilistic approach to study the effect of machined surface states on HCF behavior of a AA7050 alloy. *Int. J. Fatigue* **2018**, *116*, 473–489, doi:10.1016/j.ijfatigue.2018.06.048. [CrossRef]
29. Kitagawa, H.; Takahashi, S. Applicability of fracture mechanics to very small cracks or the cracks in the early stage. In Proceedings of the Second International Conference on Mechanical Behavior of Materials, Boston, MA, USA, 16–20 August 1976; pp. 627–631.
30. Garb, C.; Leitner, M.; Stauder, B.; Schnubel, D.; Grün, F. Application of modified Kitagawa-Takahashi diagram for fatigue strength assessment of cast Al-Si-Cu alloys. *Int. J. Fatigue* **2018**, doi:10.1016/j.ijfatigue.2018.01.030. [CrossRef]
31. Tenkamp, J.; Koch, A.; Knorre, S.; Krupp, U.; Michels, W.; Walther, F. Defect-correlated fatigue assessment of A356-T6 aluminum cast alloy using computed tomography based Kitagawa-Takahashi diagrams. *Int. J. Fatigue* **2018**, *108*, 25–34, doi:10.1016/j.ijfatigue.2017.11.003. [CrossRef]
32. Roy, M.J.; Nadot, Y.; Nadot-Martin, C.; Bardin, P.G.; Maijer, D.M. Multiaxial Kitagawa analysis of A356-T6. *Int. J. Fatigue* **2011**, *33*, 823–832, doi:10.1016/j.ijfatigue.2010.12.011. [CrossRef]
33. Beretta, S.; Romano, S. A comparison of fatigue strength sensitivity to defects for materials manufactured by AM or traditional processes. *Int. J. Fatigue* **2017**, *94*, 178–191, doi:10.1016/j.ijfatigue.2016.06.020. [CrossRef]
34. Benedetti, M.; Santus, C. Building the Kitagawa-Takahashi diagram of flawed materials and components using an optimized V-notched cylindrical specimen. *Eng. Fract. Mech.* **2020**, *224*, 106810, doi:10.1016/j.engfracmech.2019.106810. [CrossRef]
35. Patriarca, L.; Beretta, S.; Foletti, S.; Riva, A.; Parodi, S. A probabilistic framework to define the design stress and acceptable defects under combined-cycle fatigue conditions. *Eng. Fract. Mech.* **2020**, *224*, 106784, doi:10.1016/j.engfracmech.2019.106784. [CrossRef]
36. Poulin, J.R.; Kreitcberg, A.; Terriault, P.; Brailovski, V. Fatigue strength prediction of laser powder bed fusion processed Inconel 625 specimens with intentionally-seeded porosity: Feasibility study. *Int. J. Fatigue* **2020**, *132*, 105394, doi:10.1016/j.ijfatigue.2019.105394. [CrossRef]
37. Radaj, D. Geometry correction for stress intesity at elliptical cracks. *Weld. Cut.* **1977**, *29*, 198–402.
38. El Haddad, M.H.; Smith, K.N.; Topper, T.H. Fatigue Crack Propagation of Short Cracks. *J. Eng. Mater. Technol.* **1979**, *101*, 42, doi:10.1115/1.3443647. [CrossRef]
39. El Haddad, M.H.; Topper, T.H.; Smith, K.N. Prediction of non propagating cracks. *Eng. Fract. Mech.* **1979**, *11*, 573–584, doi:10.1016/0013-7944(79)90081-X. [CrossRef]

40. Chapetti, M.D. Fatigue propagation threshold of short cracks under constant amplitude loading. *Int. J. Fatigue* **2003**, *25*, 1319–1326, doi:10.1016/S0142-1123(03)00065-3. [CrossRef]
41. Maierhofer, J.; Pippan, R.; Gänser, H.P. Modified NASGRO equation for physically short cracks. *Int. J. Fatigue* **2014**, *59*, 200–207, doi:10.1016/j.ijfatigue.2013.08.019. [CrossRef]
42. Zerbst, U.; Vormwald, M.; Pippan, R.; Gänser, H.P.; Sarrazin-Baudoux, C.; Madia, M. About the fatigue crack propagation threshold of metals as a design criterion—A review. *Eng. Fract. Mech.* **2016**, *153*, 190–243, doi:10.1016/j.engfracmech.2015.12.002. [CrossRef]
43. Pippan, R.; Hohenwarter, A. Fatigue crack closure: A review of the physical phenomena. *Fatigue Fract. Eng. Mater. Struct.* **2017**, *40*, 471–495, doi:10.1111/ffe.12578. [CrossRef]
44. Suresh, S.; Ritchie, R.O. A geometric model for fatigue crack closure induced by fracture surface roughness. *Metall. Trans. A* **1982**, *13*, 1627–1631, doi:10.1007/BF02644803. [CrossRef]
45. Wasén, J.; Heier, E. Fatigue crack growth thresholds—The influence of Young's modulus and fracture surface roughness. *Int. J. Fatigue* **1998**, *20*, 737–742, doi:10.1016/S0142-1123(98)00034-6. [CrossRef]
46. Kim, J.H.; Lee, S.B. Behavior of plasticity-induced crack closure and roughness-induced crack closure in aluminum alloy. *Int. J. Fatigue* **2001**, *23*, 247–251, doi:10.1016/S0142-1123(01)00155-4. [CrossRef]
47. Suresh, S.; Zamiski, G.F.; Ritchie, D.R.O. Oxide-Induced Crack Closure: An Explanation for Near-Threshold Corrosion Fatigue Crack Growth Behavior. *Metall. Mater. Trans. A* **1981**, *12*, 1435–1443, doi:10.1007/BF02643688. [CrossRef]
48. Newman, J.A.; Piascik, R.S. Interactions of plasticity and oxide crack closure mechanisms near the fatigue crack growth threshold. *Int. J. Fatigue* **2004**, *26*, 923–927, doi:10.1016/j.ijfatigue.2004.02.001. [CrossRef]
49. Lados, D.; Apelian, D.; Paris, P.; Donald, J. Closure mechanisms in Al–Si–Mg cast alloys and long-crack to small-crack corrections. *Int. J. Fatigue* **2005**, *27*, 1463–1472, doi:10.1016/j.ijfatigue.2005.06.013. [CrossRef]
50. Murakami, Y.; Endo, M. Effects of defects, inclusions and inhomogeneities on fatigue strength. *Int. J. Fatigue* **1994**, *16*, 163–182, doi:10.1016/0142-1123(94)90001-9. [CrossRef]
51. Li, P.; Lee, P.D.; Maijer, D.M.; Lindley, T.C. Quantification of the interaction within defect populations on fatigue behavior in an aluminum alloy. *Acta Mater.* **2009**, *57*, 3539–3548, doi:10.1016/j.actamat.2009.04.008. [CrossRef]
52. Aigner, R.; Garb, C.; Leitner, M.; Stoschka, M.; Grün, F. Application of a $\sqrt{\text{area}}$ -Approach for Fatigue Assessment of Cast Aluminum Alloys at Elevated Temperature. *Metals* **2018**, *8*, 1033, doi:10.3390/met8121033. [CrossRef]
53. Aigner, R.; Leitner, M.; Stoschka, M.; Hannesschläger, C.; Wabro, T.; Ehart, R. Modification of a Defect-Based Fatigue Assessment Model for Al-Si-Cu Cast Alloys. *Materials* **2018**, *11*, 2546, doi:10.3390/ma11122546. [CrossRef]
54. Gnedenko, B. Sur la distribution limite du terme maximum d'une serie aleatoire. *Ann. Math.* **1943**, *44*, 423–453.
55. Jenkinson, A.F. The frequency distribution of the annual maximum (or minimum) values of meteorological elements. *Q. J. R. Meteorol. Soc.* **1955**, *87*, 145–158, doi:10.1002/qj.49708134804. [CrossRef]
56. Beretta, S.; Murakami, Y. Statistical analysis of defects for fatigue strength prediction and quality control of materials. *Fatigue Fract. Eng. Mater. Struct.* **1998**, *21*, 1049–1065, doi:10.1046/j.1460-2695.1998.00104.x. [CrossRef]
57. Mahdi.; Cenac, S.; Myrtene. Estimating Parameters of Gumbel Distribution using the Methods of Moments, probability weighted moments and maximum likelihood. *Rev. Mat. Teor. Apl.* **2005**, *12*, 151–156.
58. Gumbel, E.J. *Statistics of Extremes*; Columbia University Press: New York, NY, USA, 1958.
59. Murakami, Y. *Metal Fatigue: Effects of Small Defects and Nonmetallic Inclusions*, 1th ed.; Elsevier: Amsterdam, The Netherlands, 2002.
60. Murakami, Y. Material defects as the basis of fatigue design. *Int. J. Fatigue* **2012**, *41*, 2–10, doi:10.1016/j.ijfatigue.2011.12.001. [CrossRef]
61. Feikus, F.J.; Bernsteiner, P.; Gutiérrez, R.F.; Łuszczak, M. Weiterentwicklungen bei Gehäusen von Elektromotoren. *MTZ-Motortechnische Zeitschrift* **2020**, *81*, 42–47, doi:10.1007/s35146-019-0180-5. [CrossRef]
62. Campbell, J. *Complete Casting Handbook//Complete Casting Handbook: Metal Casting Processes, Metallurgy, Techniques and Design*, 2nd ed.; Elsevier: Amsterdam, The Netherlands, 2015; doi:10.1016/C2014-0-01548-1. [CrossRef]
63. DIN EN 1706. *Aluminium and Aluminium Alloys–Castings—Chemical Composition and Mechanical Properties*; German version EN 1706:2010; Beuth: Berlin, Germany

64. Sjölander, E.; Seifeddine, S. The heat treatment of Al–Si–Cu–Mg casting alloys. *J. Mater. Process. Technol.* **2010**, *210*, 1249–1259, doi:10.1016/j.jmatprotec.2010.03.020. [CrossRef]
65. Yang, H.; Ji, S.; Fan, Z. Effect of heat treatment and Fe content on the microstructure and mechanical properties of die-cast Al–Si–Cu alloys. *Mater. Des.* **2015**, *85*, 823–832, doi:10.1016/j.matdes.2015.07.074. [CrossRef]
66. Costa, A.T.; Dias, M.; Gomes, G.L.; Rocha, O.L.; Garcia, A. Effect of solution time in T6 heat treatment on microstructure and hardness of a directionally solidified Al–Si–Cu alloy. *J. Alloys Compd.* **2016**, *683*, 485–494, doi:10.1016/j.jallcom.2016.05.099. [CrossRef]
67. Toschi, S. Optimization of A354 Al-Si-Cu-Mg Alloy Heat Treatment: Effect on Microstructure, Hardness, and Tensile Properties of Peak Aged and Overaged Alloy. *Metals* **2018**, *8*, 961, doi:10.3390/met8110961. [CrossRef]
68. Han, Y.; Samuel, A.M.; Doty, H.W.; Valtierra, S.; Samuel, F.H. Optimizing the tensile properties of Al–Si–Cu–Mg 319-type alloys: Role of solution heat treatment. *Mater. Des.* **2014**, *58*, 426–438, doi:10.1016/j.matdes.2014.01.060. [CrossRef]
69. Ceschini, L.; Morri, A.; Toschi, S.; Seifeddine, S. Room and high temperature fatigue behaviour of the A354 and C355 (Al–Si–Cu–Mg) alloys: Role of microstructure and heat treatment. *Mater. Sci. Eng. A* **2016**, *653*, 129–138, doi:10.1016/j.msea.2015.12.015. [CrossRef]
70. Samuel, A.M.; Doty, H.W.; Valtierra, S.; Samuel, F.H. Relationship between tensile and impact properties in Al–Si–Cu–Mg cast alloys and their fracture mechanisms. *Mater. Des.* **2014**, *53*, 938–946, doi:10.1016/j.matdes.2013.07.021. [CrossRef]
71. do Lee, C. Effect of T6 heat treatment on the defect susceptibility of fatigue properties to microporosity variations in a low-pressure die-cast A356 alloy. *Mater. Sci. Eng. A* **2013**, *559*, 496–505, doi:10.1016/j.msea.2012.08.131. [CrossRef]
72. Zhu, M.; Jian, Z.; Yang, G.; Zhou, Y. Effects of T6 heat treatment on the microstructure, tensile properties, and fracture behavior of the modified A356 alloys. *Mater. Des.* **2012**, *36*, 243–249, doi:10.1016/j.matdes.2011.11.018. [CrossRef]
73. Boileau, J.M.; Allison, J.E. The effect of solidification time and heat treatment on the fatigue properties of a cast 319 aluminum alloy. *Metall. Trans.* **2003**, *34*, 1807–1820, doi:10.1007/s11661-003-0147-4. [CrossRef]
74. Fabrizi, A.; Capuzzi, S.; de Mori, A.; Timelli, G. Effect of T6 Heat Treatment on the Microstructure and Hardness of Secondary AlSi9Cu3(Fe) Alloys Produced by Semi-Solid SEED Process. *Metals* **2018**, *8*, 750, doi:10.3390/met8100750. [CrossRef]
75. Aigner, R.; Leitner, M.; Stoschka, M. On the mean stress sensitivity of cast aluminium considering imperfections. *Mater. Sci. Eng. A* **2019**, *758*, 172–184, doi:10.1016/j.msea.2019.04.119. [CrossRef]
76. Leitner, M.; Garb, C.; Remes, H.; Stoschka, M. Microporosity and statistical size effect on the fatigue strength of cast aluminium alloys EN AC-45500 and 46200. *Mater. Sci. Eng. A* **2017**, *707*, 567–575, doi:10.1016/j.msea.2017.09.023. [CrossRef]
77. Vandersluis, E.; Ravindran, C. Comparison of Measurement Methods for Secondary Dendrite Arm Spacing. *Metallogr. Microstruct. Anal.* **2017**, *6*, 89–94, doi:10.1007/s13632-016-0331-8. [CrossRef]
78. Boileau, J.M.; Zindel, J.W.; Allison, J.E. The Effect of Solidification Time on the Mechanical Properties in a Cast A356-T6 Aluminum Alloy. *SAE Trans.* **1997**, *106*, 63–74.
79. Zhang, L.Y.; Jiang, Y.H.; Ma, Z.; Shan, S.F.; Jia, Y.Z.; Fan, C.Z.; Wang, W.K. Effect of cooling rate on solidified microstructure and mechanical properties of aluminium-A356 alloy. *J. Mater. Process. Technol.* **2008**, *207*, 107–111, doi:10.1016/j.jmatprotec.2007.12.059. [CrossRef]
80. Ceschini, L.; Boromei, I.; Morri, A.; Seifeddine, S.; Svensson, I.L. Microstructure, tensile and fatigue properties of the Al–10%Si–2%Cu alloy with different Fe and Mn content cast under controlled conditions. *J. Mater. Process. Technol.* **2009**, *209*, 5669–5679, doi:10.1016/j.jmatprotec.2009.05.030. [CrossRef]
81. Zhang, B.; Chen, W.; Poirier, D.R. Effect of solidification cooling rate on the fatigue life of A356.2-T6 cast aluminium alloy. *Fatigue Fract. Eng. Mater. Struct.* **2000**, *23*, 417–423, doi:10.1046/j.1460-2695.2000.00299.x. [CrossRef]
82. Gerbe, S.; Krupp, U.; Michels, W. Influence of secondary dendrite arm spacing (SDAS) on the fatigue properties of different conventional automotive aluminum cast alloys. *Frat. Integrità Strutt.* **2019**, *13*, 105–115, doi:10.3221/IGF-ESIS.48.13. [CrossRef]

83. Leitner, H. Simulation des Ermüdungsverhaltens von Aluminiumgusslegierungen. Ph.D. Thesis, Montanuniversität Leoben, Leoben, Austria, 2001.
84. Garb, C.; Leitner, M.; Grün, F. Application of $\sqrt{\text{area}}$-concept to assess fatigue strength of AlSi7Cu0.5Mg casted components. *Eng. Fract. Mech.* **2017**, *185*, 61–71. doi:10.1016/j.engfracmech.2017.03.018. [CrossRef]
85. ASTM International E 739. Standard Practice for Statistical Analysis of Linear or Linearized Stress-Life (S-N) and Strain Life (E-N) Fatigue Data, ASTM International: West Conshohocken, PA, 1998.
86. Dengel, D.; Harig, H. Estimation of the fatigue limit by progressively-increasing load tests. *Fatigue Fract. Eng. Mater. Struct.* **1980**, *3*, 113–128, doi:10.1111/j.1460-2695.1980.tb01108.x. [CrossRef]
87. Garb, C.; Leitner, M.; Grün, F. Effect of elevated temperature on the fatigue strength of casted AlSi8Cu3 aluminium alloys. *Procedia Struct. Integr.* **2017**, *7*, 497–504, doi:10.1016/j.prostr.2017.11.118. [CrossRef]
88. Wang, Q.; Apelian, D.; Lados, D. Fatigue behavior of A356/357 aluminum cast alloys. Part II—Effect of microstructural constituents. *J. Light Met.* **2001**, *1*, 85–97, doi:10.1016/S1471-5317(00)00009-2. [CrossRef]
89. Wang, Q.; Apelian, D.; Lados, D. Fatigue behavior of A356-T6 aluminum cast alloys. Part I—Effect of casting defects. *J. Light Met.* **2001**, *1*, 73–84, doi:10.1016/S1471-5317(00)00008-0. [CrossRef]
90. Åman, M.; Okazaki, S.; Matsunaga, H.; Marquis, G.B.; Remes, H. The effect of interacting small defects on the fatigue limit of a medium carbon steel. *Procedia Struct. Integr.* **2016**, *2*, 3322–3329, doi:10.1016/j.prostr.2016.06.414. [CrossRef]
91. Massey, F.J., Jr. The Kolmogorov-Smirnov test for goodness of fit. *J. Am. Stat. Assoc.* **1951**, *46*, 68–78.

© 2020 by the authors. Licensee MDPI, Basel, Switzerland. This article is an open access article distributed under the terms and conditions of the Creative Commons Attribution (CC BY) license (http://creativecommons.org/licenses/by/4.0/).